Resolution Enhancement of UWB Time-Reversal Microwave Imaging in Dispersive Environments

Loukas Xanthos, Mehmet E. Yavuz, Ryutaro Himeno, Hideo Yokota, Fumie Costen, *Senior Member, IEEE*

***Abstract*—Time Reversal (TR) techniques allow optimal refocusing of ultrawideband (UWB) electromagnetic waves in complex propagation environments, due to the invariance of the wave equations. Propagation of electromagnetic waves through dispersive or lossy media breaks this invariance. Consequently, such media degrade the refocusing ability of TR techniques. In this work, we propose a novel algorithm for the enhancement of the UWB TR microwave imaging resolution in dispersive environments. The presented algorithm takes into account the frequency-dependent complex permittivity of the propagation medium across the entire bandwidth of the UWB pulse. Using this complex permittivity, it models the medium-, time-, and frequency- dependent attenuation in the wavelet domain to create inverse filters which compensate for the effects of the attenuation. This is the first algorithm that constructs inverse filters in the wavelet domain using the complex permittivity of the dispersive propagation medium across the entire bandwidth, rather than at a center frequency, of the excitation pulse. We also introduce a smart scaling concept to minimize undesired noise amplification. While our proposed approach is agnostic to the application scenario and thus could be utilized in various disciplines, we apply it in a biomedical imaging scenario and achieve enhancement in the resolution of UWB microwave TR imaging of a simulated brain tumor inside the digital human phantom (DHP).**

***Index Terms*—Microwave imaging, focusing, biomedical imaging, radar signal processing, dispersive media, time reversal (TR)**

I. Introduction

THE time-reversal (TR) method exploits the invariance of the wave equation under a time-reversal operation in lossless and stationary media to refocus time-reversed signals back to their source. The TR method works by recording and time-reversing the distorted wave-field coming from a source (active or passive) at the focal point of interest [1]. As a result, optimal spatial and temporal refocus is achieved under the condition that the propagation media are lossless. The TR method can be applied on ultra-wideband (UWB) signals and harness multipaths to improve the refocusing precision and to achieve superresolution [2]–[6], i.e. a spatial resolution much finer than achievable in free space.

L. Xanthos and F. Costen are with the Department of Electrical and Electronic Engineering, The University of Manchester, Manchester, U.K. (email: loukas.xanthos@manchester.ac.uk and fumie.costen@manchester.ac.uk).

M. E. Yavuz, Hillsboro, Oregon, USA. (email: yavuz.5@osu.edu)

R. Himeno is with Head Office for Information Systems and Cybersecurity, RIKEN, Saitama, Japan.

H. Yokota and F. Costen are with the Image Processing Research Team, Center for Advanced Photonics, RIKEN, Saitama, Japan.

Color version of the figures in this paper are available online at http://ieeexplore.ieee.org .

Additional research data supporting this publication are available from the Zenodo repository at doi:10.5281/zenodo.3910784 .

The TR method has found several applications in recent years, such as acoustics for brain therapy, non-destructive testing, under-water telecommunications, fault diagnosis in wire networks [7]. In electromagnetics, the TR techniques have been applied in radar imaging including Ground Penetrating Radar (GPR) [2], [8], [9], in communications [10]–[12] and in biomedical applications [13]–[15]. Microwave imaging utilizing TR aimed for microwave breast cancer detection has been studied in [13], [16]–[18] and references therein.

TR techniques in electromagnetics employ a set of transmit-receive (Tx/Rx) elements, called the TR array (TRA) [8]. Each TRA element receives the signals originating from the source. These signals are recorded, time-reversed, and then sent back to the propagation medium by each TRA element simultaneously, to achieve refocusing around the original source location. In the case of a scatterer acting as a passive source, the propagation environment can first be illuminated by one of the TRA elements.

The TR invariance of the wave equation breaks in the presence of lossy propagation media [3], [19]. While the TR process itself can compensate for the additional phase shift incurred by dispersion, it cannot compensate for the amplitude attenuation the TR signals undergo during both forward and backpropagation [3], [19]. This attenuation degrades the resolution of the TR refocusing relative to the lossless and non-dispersive case. Inverse filters can be employed to compensate for the attenuation of the TR signals. In the case of random and/or inhomogeneous propagation media, approximate inverse filters can be used [3]. This practice can be applied for TR-based microwave imaging applications where the obtainment of qualitative radar images, rather than quantitative fields, is acceptable [20].

The work in [19] compensates the dispersion in UWB TR applications by making use of time-dependent inverse filtering with short-time Fourier transforms (STFT), to improve the refocusing of time-reversed electromagnetic waves. [19] constructs the inverse filters by comparing the solution of the wave equation in the dispersive propagation medium at various propagation distances against a corresponding nondispersive test medium. There are three major drawbacks to adopting the inverse filter production proposed by [19]. First, it is empirical, as it requires a manual examination of the spectral density of the received signals to assess whether the noise levels at individual frequencies are unacceptably high, depending on the application. The amplification of noise-affected frequencies is minimized by manually adjusting the filtering process. Second, it assumes perfect knowledge of the dispersive characteristics of the propagation media. Finally, it is time consuming, as it

implies prior realization of one experiment with the lossless test medium.

Later, [21] extended the method in [19] by introducing a threshold approach to minimize the amplification of the noise in the inverse filters in [19]. The work in [21] investigates the application of different window types and lengths to optimize the selection of the parameters of the STFT filters. While the noise reduction process is automated by [21], the requirements of performing one extra experiment with the non-dispersive test medium and of perfect knowledge of the dispersive characteristics of the propagation media persist. Another limitation imposed by [21] is that it assumes knowledge of the location of the scatterers during the optimization process, which may not be available in real-life applications. Besides, both [21] and [19] consider only point-like perfect electric conductor (PEC) scatterers.

More recently, the authors in [22] propose an adaptive-window scheme based on the continuous wavelet transform (CWT) of discrete-time signals received by a TRA. Hence, [22] performs the discrete-time wavelet transform (DTWT) [23] of the received signals. The wavelet transform method applies a temporally long window to the received signals at the lower frequencies of the spectrum (large scales) and a temporally short window at the higher frequencies of the spectrum (small scales). Therefore, it is well-suited for time-dependent filter implementations in terms of time and frequency localization [22]. The method in [22] uses stabilized approximate inverse filters in the wavelet domain to increase the resolution of the TR refocusing of UWB signals. Each of these stabilized inverse filters is a model of the attenuation in the wavelet domain and is produced using the complex permittivity of the propagation medium, which is assumed to be known. Using these inverse filters, [22] compensates the attenuation due to the medium and thus results to more precise TR refocusing. The compensation of attenuation in the case of [22] is not exact. Besides, the work in [22] is focused on the enhancement of the TR refocusing resolution, and hence on the qualitative improvement of the radar image. It does not aim to preserve the energy of the interrogating pulse before and after the inverse filtering process and it performs no such study. The work in [22] uses the value of the complex permittivity of one dominant propagation medium at the center frequency of the interrogating UWB pulse to create the inverse filters without taking into account the frequency dependency of propagation media.

In this work, we propose an algorithm for the resolution enhancement of UWB TR imaging in lossy propagation media, such as dispersive human tissues. While brain imaging is considered in this paper, our algorithm can be applied to other disciplines involving dispersive media, such as GPR, through-the-wall imaging, etc. Our work corrects and improves the adaptive-window scheme method proposed in [22]. The approach in [22] associates the wavelet transform scales to frequencies in an arbitrary way, which leads to unreliable performance. We correct this by proposing the use of a different method to associate wavelet scales with Fourier frequencies. The method our work uses to associate wavelet scales with Fourier frequencies is derived mathematically and has been employed by existing wavelet transform-related literature. The main novelty introduced by our algorithm is that it incorporates the frequency-dependent complex permittivity of the propagation medium across the *whole* frequency spectrum, rather than at a center frequency, of the interrogating UWB pulse, for the first time to our knowledge, to construct a scale-, and hence, frequency-dependent model of the attenuation which the pulse undergoes during the TR forward propagation. Using this model, our algorithm constructs stabilized inverse filters and enhances the refocusing resolution of time-reversed UWB electromagnetic waves in dispersive media. Furthermore, our method applies smart scaling that prevents the amplification of unwanted noise at frequencies which are not part of the spectrum of interest of the UWB pulse. The method in [22] fails to do so, as it performs amplification over a part of the noise spectrum instead of selecting the bandwidth portion that corresponds to the signal and it hence breaks the TR refocusing process. Our algorithm is in principle general and agnostic to application scenario. In this paper, we choose the brain tumor detection scenario to demonstrate the performance of our work. While clutter removal techniques can be utilized alongside to improve the overall system performance further, we leave this as part of future work and here we focus on the resolution enhancement algorithm for UWB microwave TR imaging regardless of clutter removal techniques.

II. Resolution Enhancement of UWB TR Imaging in Dispersive Media

Let $x(t)$ be the signal received by one TRA element. $x(t)$ is sampled and represented in discrete time domain as

$$x[n] = x(nT_\mathrm{s}) \qquad n = 0, 1, 2, \ldots, N-1 \tag{1}$$

where T_s is the sampling period and N is the total number of sampling points in the time domain signal. We use the complex Morlet function as the analyzing (*mother*) wavelet for the DTWT of $x[n]$, following [22]. Let $\psi_0(\eta)$

$$\psi_0(\eta) = \frac{1}{\sqrt[4]{\pi}} e^{\jmath\omega_\mathrm{M}\eta} e^{-\eta^2/2} \tag{2}$$

be the mother wavelet function where $\omega_\mathrm{M} = 2\pi f_\mathrm{M}$ is the central angular frequency of the mother wavelet, f_M is the corresponding frequency, and $\jmath = \sqrt{-1}$. For (2), a value of $\omega_\mathrm{M} > 5$ must be chosen so that $\psi_0(t)$ is approximately admissible [24]. The value $\omega_\mathrm{M} = 6$ is commonly employed in practice [25]–[27], which we also use following [22]. We express $\psi_0(t)$ in the scaled discrete frequency domain as [25]

$$\Psi_0[a_j\omega_k] = \begin{cases} \frac{1}{\sqrt[4]{\pi}} e^{-\frac{1}{2}(a_j\omega_k - \omega_\mathrm{M})^2} & \omega_k > 0 \\ 0 & \text{otherwise} \end{cases} \tag{3}$$

where a_j is the scale factor associated with each individual scale with index $j = 0, 1, \ldots, J$, given as a relation between the smallest resolvable scale a_0, the index j, and the scale step Δj by

$$a_j = a_0 \cdot 2^{j\Delta j}. \tag{4}$$

We set a_0 so that the equivalent Fourier period is $2T_\mathrm{s}$ [25]. ω_k is the k-th harmonic of the fundamental frequency which is defined as

$$\omega_k = \begin{cases} \dfrac{2\pi k}{NT_\mathrm{s}} & k \leq \dfrac{N}{2} \\ -\dfrac{2\pi(N-k)}{NT_\mathrm{s}} & k > \dfrac{N}{2} \end{cases} \tag{5}$$

and $k = 0, 1, 2, \ldots, N-1$ is the frequency bin. The index of the largest scale J is computed by [25]

$$J = \left\lceil \frac{1}{\Delta j} \log_2\left(\frac{NT_\mathrm{s}}{a_0}\right) \right\rceil \tag{6}$$

where $\lceil\ \rceil$ is the ceiling function. Δj controls the scale discretization. Smaller values of Δj achieve finer discretization of the scale parameter, which typically results in a higher-fidelity signal analysis. However, with smaller values of Δj, the amount of required computation increases, because there is a larger total number of scales and the DTWT is computed at each scale. In this work, we assign $\Delta j = 0.025$ following [22].

We normalize the wavelet function so that it has unit energy at each scale and to guarantee that the DTWTs at each a_j are comparable to each other [25]:

$$\Psi[a_j\omega_k] = \sqrt{\frac{2\pi a_j}{T_\mathrm{s}}}\Psi_0[a_j\omega_k]. \tag{7}$$

Our compensation process first converts $x[n]$ to the wavelet domain. The DTWT of the signal $x[n]$ is defined as

$$X[a_j, n] = \sum_{k=0}^{N-1}\left[\frac{1}{N}\left(\sum_{\tau=0}^{N-1} x[\tau]e^{-\jmath\tau\frac{2\pi k}{N}}\right)\Psi^*[a_j\omega_k]e^{\jmath\omega_k nT_\mathrm{s}}\right] \tag{8}$$

where * represents the complex conjugate.

We apply inverse filtering to $X[a_j, n]$ in the wavelet domain to compensate for the effects of the attenuation caused by the dispersive medium. To form the inverse filters, we compute the attenuation corresponding to $X[a_j, n]$. We assume a single point source of band-limited electromagnetic radiation placed inside a homogeneous and isotropic non-magnetic dispersive medium of infinite size. Let the complex permittivity of the linear and lossy propagation medium be noted as $\epsilon(f) = \epsilon'(f) - \jmath\epsilon''(f) \triangleq \epsilon_0\epsilon_\mathrm{r}(f)$ in F/m where ϵ_0 is the vacuum permittivity, ϵ_r is the complex relative permittivity, f is the frequency in Hz, and $\epsilon'(f), \epsilon''(f)$ are real functions of f. We use the one-pole Debye relaxation model for the human tissues [28]

$$\epsilon_\mathrm{r}(f) = \epsilon_\infty + \frac{\epsilon_\mathrm{s} - \epsilon_\infty}{1 + \jmath 2\pi f\tau_\mathrm{D}} - \jmath\frac{\sigma}{2\pi f\epsilon_0} \tag{9}$$

where ϵ_∞ is the optical relative permittivity, ϵ_s is the static relative permittivity, τ_D is the relaxation time, σ is the static conductivity.

The attenuation factor of the propagation medium can be expressed as [29]

$$\alpha(f) = 2\pi f\frac{1}{\sqrt{2}c}\left[\sqrt{1 + \left(\frac{\epsilon''(f)}{\epsilon'(f)}\right)^2} - 1\right]^{1/2} \tag{10}$$

where $\alpha(f)$ is the attenuation factor associated with f in Np/m and c is the speed of light in the propagation medium.

Suppose a sinusoidal signal with frequency f at propagation distance r from the excitation source. This signal is subject to attenuation $\varphi(f, r)$ which is given by [29]

$$\varphi(f, r) = \exp(-\alpha(f)\cdot r). \tag{11}$$

This signal is also subject to an additional phase shift of $e^{-\jmath\beta(f)r}$, where $\beta(f)$ is the phase constant. Since the TR operation corresponds to phase conjugation in frequency domain, we are not concerned with this additional phase shift, as the TR method automatically compensates any phase distortion that affects the forward propagation [19]. We can express r in terms of time as

$$r(t) = c\cdot t \tag{12}$$

where t is the time of travel of the electric field plane wave. Using (12), (11) becomes

$$\begin{aligned}\varphi(f, t) &= \exp(-\alpha(f)\cdot r(t)) \\ &= \exp\left(-\frac{2\pi f}{\sqrt{2}}\left[\sqrt{1 + \left(\frac{\epsilon''(f)}{\epsilon'(f)}\right)^2} - 1\right]^{1/2}\cdot t\right).\end{aligned} \tag{13}$$

We model (13) in wavelet domain as $\Phi(a_j, t)$. To express $\Phi(a_j, t)$ algebraically, we consider the relation between a_j and f. When (2) is used as the mother wavelet, an analytical relation between each scale factor a_j and one equivalent Fourier frequency $f = f_\mathrm{e}(\omega_\mathrm{M}, a_j)$ can be found. This relation can be obtained by taking the wavelet transform of a complex sinusoid at a known frequency and deriving the scale a_j at which the wavelet energy density is maximized, following the method in [30]. This yields [25], [30], [31]

$$f_\mathrm{e}(\omega_\mathrm{M}, a_j) = \frac{\omega_\mathrm{M} + \sqrt{2 + {\omega_\mathrm{M}}^2}}{4\pi a_j}. \tag{14}$$

The derivation of (14) is provided in the Appendix. Hence we express our wavelet domain model of the forward attenuation as

$$\begin{aligned}\Phi(a_j, t) &= \exp\Big(-\alpha\big(f_\mathrm{e}(\omega_\mathrm{M}, a_j)\big)\cdot r(t)\Big) \\ &= \exp\Bigg(-\frac{2\pi f_\mathrm{e}(\omega_\mathrm{M}, a_j)}{\sqrt{2}} \\ &\quad\cdot\left[\sqrt{1 + \left(\frac{\epsilon''\big(f_\mathrm{e}(\omega_\mathrm{M}, a_j)\big)}{\epsilon'\big(f_\mathrm{e}(\omega_\mathrm{M}, a_j)\big)}\right)^2} - 1\right]^{1/2}\cdot t\Bigg).\end{aligned} \tag{15}$$

By sampling (15) we have that

$$\Phi[a_j,n]=\exp\left(-\frac{2\pi f_{\mathrm{e}}(\omega_{\mathrm{M}},a_j)}{\sqrt{2}}\cdot\left[\sqrt{1+\left(\frac{\epsilon''\big(f_{\mathrm{e}}(\omega_{\mathrm{M}},a_j)\big)}{\epsilon'\big(f_{\mathrm{e}}(\omega_{\mathrm{M}},a_j)\big)}\right)^2}-1\right]^{1/2}\cdot nT_{\mathrm{s}}\right). \quad (16)$$

The work in [22] does not make use of relation (14). Conversely, [22] dilates the central frequency of $x[n]$, f_{c}, by each scale factor to arbitrarily associate each scale factor to a frequency, as in

$$f=\frac{f_{\mathrm{c}}}{a_j}. \quad (17)$$

(17) has no physical meaning relating to the frequency content of $X[a_j,n]$ for constant a_j. In addition, the attenuation model in [22] uses the value for the permittivity of one medium only at f_{c} instead of taking into account the functional relationship of ϵ and f, and therefore ϵ and a_j. Thus, the model of attenuation in [22] is invalid for non-monochromatic waves propagating in dispersive media. With (16), our approach considers the effect of the attenuation on $x[n]$ across all scales – and hence, frequencies – of interest of $x[n]$.

To compensate for the effects of the frequency- and time-dependent attenuation, we construct inverse filters in the wavelet domain as in

$$H[a_j,n]=\frac{1}{\Phi[a_j,n]}. \quad (18)$$

As the excitation wave travels beyond a certain distance from the source, its magnitude at high frequencies (small scales) becomes weaker than the noise. The inverse filters in (18) would amplify noise-dominated scales by an exponential function of time. To minimize such amplification of noise after long travel times, we stabilize (18) and form the stabilized inverse filters [32]–[34] of

$$H_{\mathrm{s}}[a_j,n]=\frac{\Phi[a_j,n]}{\Phi^2[a_j,n]+s^2} \quad (19)$$

where s^2 is the real positive stabilization parameter. This parameter can be set empirically [33]–[35]. Alternatively, s^2 can be set as a ratio of variances of signal and noise, as a measure of signal-to-noise ratio (SNR) [33]. The system is stable with a fixed value of $s=10^{-7}$ in all our simulations.

We produce the compensated wave sequence $Y[a_j,n]$ by applying $H_{\mathrm{s}}[a_j,n]$ on $X[a_j,n]$ in the wavelet domain as

$$Y[a_j,n]=\begin{cases}H_{\mathrm{s}}[a_j,n]X[a_j,n] & \text{if } f_{\min}\le f_{\mathrm{e}}(\omega_{\mathrm{M}},a_j)\le f_{\max}\\ X[a_j,n] & \text{otherwise}\end{cases} \quad (20)$$

where $f_{\min}$ and $f_{\max}$ are the minimum and maximum frequencies of the spectrum of the source excitation respectively. We do not apply the inverse filters outside of the frequency range of interest to avoid amplification of noise outside this range. With (20) our approach takes into account the entire frequency range of interest for the stabilized inverse filtering of $x[n]$.

The work in [22] sets H_{s} to 1 only for $0\le j\le J/2$ to prevent the amplification of high frequency noise. While this choice of scale indices selects the higher part of the frequency spectrum used by the DTWT, it does not specify the exact frequency range where we are not interested. Consequently, the amplification of noise beyond $f_{\max}$ and below $f_{\min}$ is possible in [22].

Finally, we obtain the compensated signal in time domain $y[n]$ by taking the Inverse DTWT (IDTWT) of $Y[a_j,n]$ as in

$$y[n]=\frac{\Delta j {T_{\mathrm{s}}}^{1/2}}{C_\delta\psi_0(0)}\sum_{j=0}^{J}\frac{\mathrm{Re}\{Y[a_j,n]\}}{\sqrt{a_j}} \quad (21)$$

where C_δ is a constant for each wavelet function and $\mathrm{Re}\{\ \}$ is the real part of its complex argument. For the Morlet wavelet of (2), C_δ is calculated as [25]

$$C_\delta=\frac{\Delta j {T_{\mathrm{s}}}^{1/2}}{\psi_0(0)}\sum_{j=0}^{J}\frac{\mathrm{Re}\left\{\sum_{k=0}^{N-1}\Psi^*[a_j\omega_k]/N\right\}}{\sqrt{a_j}}. \quad (22)$$

We apply the same process for each $x(t)$ received at each TRA element before the backpropagation stage. Fig. 1 summarizes our proposed approach in a block diagram. When we utilize our filter in an inhomogeneous scenario, we set ϵ in (15) to the complex permittivity of the dominant medium. We define as dominant the medium which covers the largest area of the propagation space between the TRA and the electric field source.

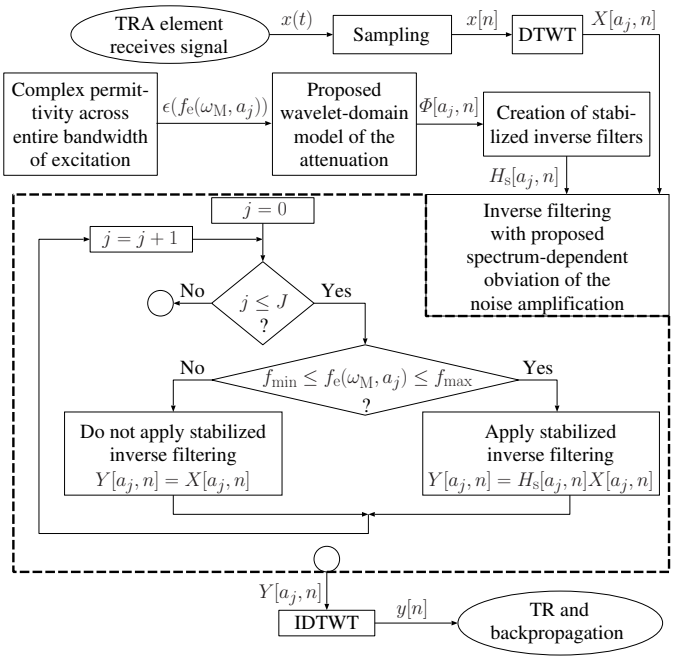

Fig. 1. Block diagram of our proposed algorithm for the resolution enhancement of UWB TR imaging in dispersive media.

III. Numerical Experiments

Brain tumors are one of the deadliest of all forms of cancer [36], [37]. Microwave imaging of the brain is challenging because of complex layered tissues inside the head [38], which attenuate electromagnetic signals propagating through them. We apply the TR imaging technique with our proposed resolution enhancement method to locate a brain tumor in the Digital Human Phantom (DHP). The purpose of these numerical simulations is to evaluate the improvement in resolution by using our method on a practical case scenario which involves propagation through multiple dispersive human tissues.

The DHP was provided by RIKEN (Saitama, Japan) under nondisclosure agreement between RIKEN and The University of Manchester (Manchester, U.K.). Its usage was approved by the RIKEN ethical committee. The DHP has 1 mm resolution and contains 52 segmented tissues. We fitted the one-pole Debye parameters of human tissues [39] using the measurements provided in [40] and [41]. The Debye media parameters for human tissues are presented in [42].

A. Simulation Settings

This scenario involves the head of the DHP. We illustrate the simulation setup in Fig. 2 (3D graphic produced by using [43], [44]). A 3D frequency-dependent finite difference time domain ((FD)^{2}TD) [45] space of size 321 cells $\times$ 297 cells $\times$ 160 cells was used for our simulations. The complex frequency-shifted perfectly matched layer (CFS-PML) absorbing boundary conditions [46] are used with a 32-cell layer. The FDTD space is uniformly sampled with a spatial step of $\Delta h \triangleq \Delta x = \Delta y = \Delta z = 1$ mm. The temporal step $\Delta t \equiv T_\mathrm{s}$ for the FDTD simulation is set to 1.9245 ps.

We place 11 TRA elements on the skin as in Fig. 2. The interrogating TRA element is at location $(x_{\mathrm{d}_0}, y_{\mathrm{d}_0}, z_{\mathrm{d}_0}) = (175, 71, 108)$, where x_d, y_d, z_d are the grid cell coordinates in the x, y and z directions respectively. It is excited with a first derivative of a Gaussian pulse, with a center frequency f_c of 3 GHz. The excitation pulse covers a frequency range of $f_\mathrm{min} \leq f \leq f_\mathrm{max}$ with $f_\mathrm{min} = 700$ MHz and $f_\mathrm{max} = 6.2$ GHz. Frequencies $f_\mathrm{min}, f_\mathrm{max}$ satisfy $S(f_\mathrm{min}) = S(f_\mathrm{max}) = e^{-1} \times S(f_\mathrm{c}) = e^{-1}$ [21] where $S(f)$ is the normalized frequency spectrum of the excitation signal. We observe E_z at each TRA element. We simulate an SNR of 45 dB by applying Additive White Gaussian Noise (AWGN) to $x[n]$ received at each TRA element.

In Table I, we list the Debye media parameters which we use in this numerical experiment. We simulate the tumor as a sphere with a diameter of 7 mm located on the white matter (right hemisphere) as in Fig. 2. We set the relative permittivity ${\epsilon_\mathrm{r}}^{\mathrm{cancer}}$ of the brain tumor as [47] ${\epsilon_\mathrm{r}}^{\mathrm{cancer}}(f) = {\epsilon_\mathrm{r}}^{\mathrm{wh.\ matter}}(f) \times (1 + 30\%)$, where ${\epsilon_\mathrm{r}}^{\mathrm{wh.\ matter}}(f)$ is the complex relative permittivity of healthy white matter [42].

We carry out the TR experiment using no filter, using the proposed approach, and using the method in [22]. We use the time-reversed perturbed fields during the TR back-propagation [13]. These fields are obtained by subtracting the forward scattered signals computed using the scenario geometry with and without the target object as also followed in other works in the literature, such as [16], [17], [48], [49]. The time-reversed perturbed fields are back-propagated inside a geometry identical to Fig. 2 but without the tumor. Note that we follow the *same* procedure described above for all the methods examined in this manuscript to obtain *consistent* comparisons and demonstrate the relative improvement. To objectively decide the time of refocusing, and hence perform a fair comparison of the refocusing achieved by these methods, we use the minimum entropy criterion on E_z in a region of interest of the unfiltered TR experiment [13]. Both resolution enhancement algorithms are independent of both the region of interest and the time of refocusing. We employ the inverse varimax norm of E_z, (23), as measure of entropy [16], [17], [50], with

$$\Xi(E_z^n) = \frac{\left[\sum_{x_\mathrm{d}, y_\mathrm{d}} E_z^{n\,2}(x_\mathrm{d}, y_\mathrm{d}, z_{\mathrm{d}_0})\right]^2}{\sum_{x_\mathrm{d}, y_\mathrm{d}} E_z^{n\,4}(x_\mathrm{d}, y_\mathrm{d}, z_{\mathrm{d}_0})}. \tag{23}$$

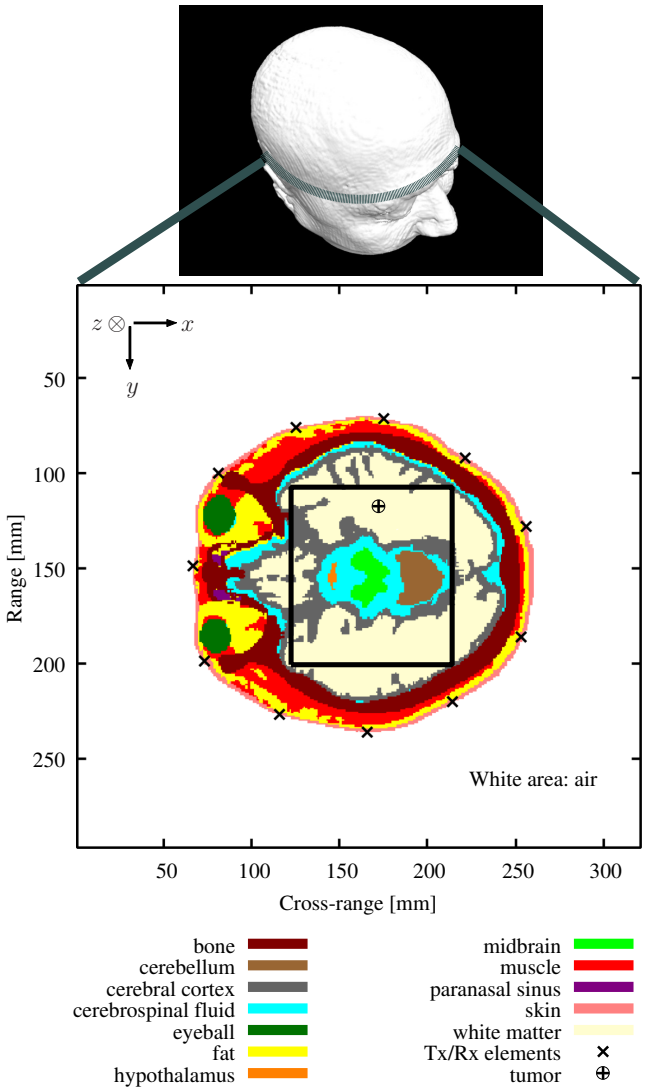

Fig. 2. The geometry of the simulation scenario. The black rectangle indicates the region of interest.

TABLE I
DEBYE PARAMETERS OF DHP MEDIA

Propagation medium	σ [S/m]	ϵ_{s}	ϵ_{∞}	τ_{D} [ps]
Bone	0.104	14.169	7.363	0.341
Cerebellum	0.826	58.155	35.195	0.683
Cerebral cortex	0.595	56.444	33.057	0.352
Cerebrospinal fluid	2.144	70.400	33.148	0.182
Eyeball	1.445	67.711	10.308	8.271
Fat	0.037	5.531	3.998	0.236
Hypothalamus	0.595	56.444	33.057	0.352
Midbrain	0.348	41.281	24.371	0.336
Muscle	0.747	56.932	28.001	0.187
Paranasal sinus	0.000	1.000	1.000	0.000
Skin	0.541	47.930	29.851	0.436
White matter	0.348	41.281	24.371	0.336

We compute $\Xi(E_z^n)$ inside the region of interest, away from the TRA elements, to minimize the effect the transmitting elements have on the minimum entropy selection process during backpropagation. We quantify the spatial resolution for each method. We expect that our approach presents the best resolution of the TR refocusing. For both resolution enhancement methods, we use the frequency-dependent white matter tissue as the dominant medium for the inverse filters.

B. Results

The normalized $|E_z|$ distribution with conventional TR imaging without inverse filtering, one with our resolution enhancement approach, and one with the approach in [22] are presented in Figs. 3, 4, and 5, respectively.

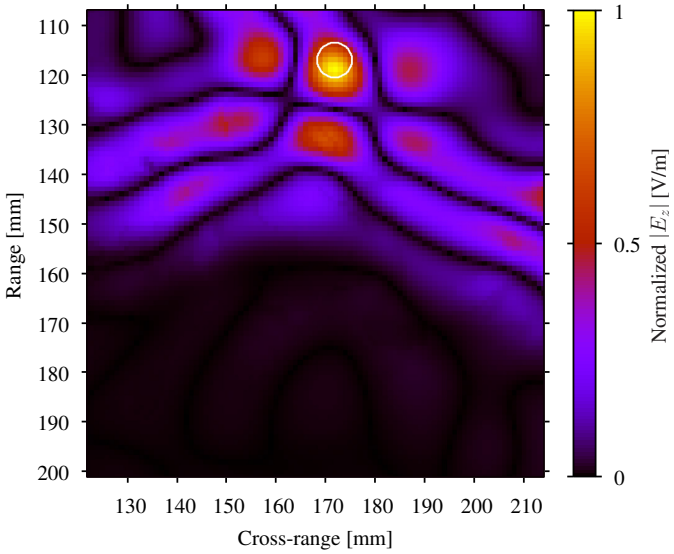

Fig. 3. Normalized $|E_z|$ distribution inside the region of interest at the time of refocusing without applying any resolution enhancement method. The white circle represents the tumor.

The method in [22] failed to achieve refocusing. Instead, it resulted in artifacts in Fig. 5 which were higher in intensity near the TRA elements. The algorithm in [22] uses (17) to calculate f associated with each a_j. Thus, it associated the

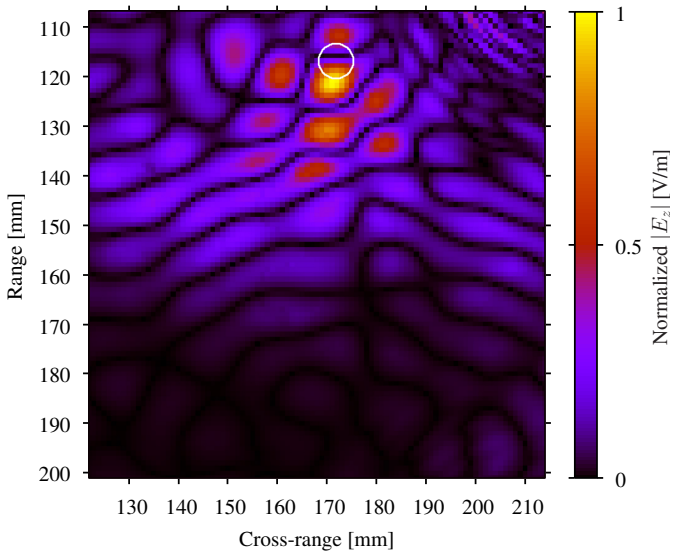

Fig. 4. Normalized $|E_z|$ distribution inside the region of interest at the time of refocusing using our resolution enhancement approach. The white circle represents the tumor.

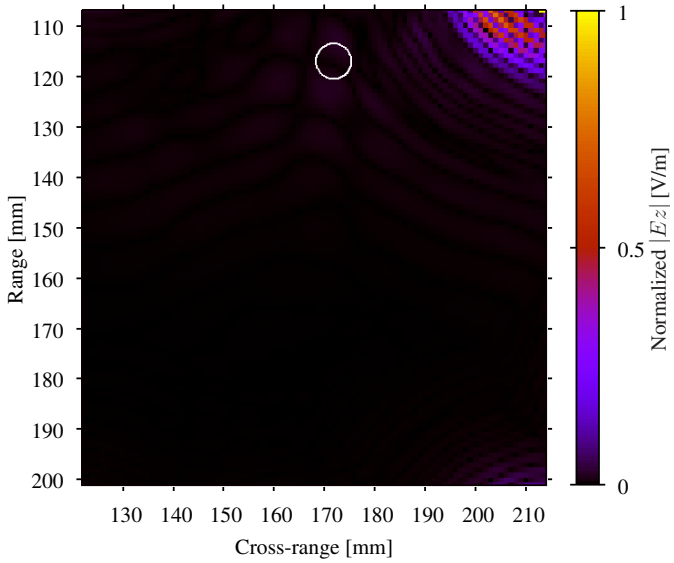

Fig. 5. Normalized $|E_z|$ distribution inside the region of interest at the time of refocusing using the method from [22]. The white circle represents the tumor.

non-rejected scales to a frequency range from $3.43 \cdot 10^{17}$ Hz to $2.31 \cdot 10^{19}$ Hz. This frequency range does not belong to the frequency spectrum of interest of $x(t)$. Moreover, the calculation of $\alpha(f)$ by the method in [22] is proportional to f (as [22] evaluates ϵ' and ϵ'' only at $f = f_{\mathrm{c}}$). Therefore the value of $\alpha(f)$ with [22] becomes 10 orders of magnitude larger than the true value of $\alpha(f)$. Thus [22] carries out unreliable computation of $\Phi[a_j, n]$ and of $H_{\mathrm{s}}[a_j, n]$, resulting in the breaking of the TR process. Our proposed filter compensates for the effect of the losses caused by the dispersive human tissues and thus yields more precise spatial focusing than the non-enhanced TR method.

Figs. 6 and 7 present the cross-section of the $|E_z|$ distribu-

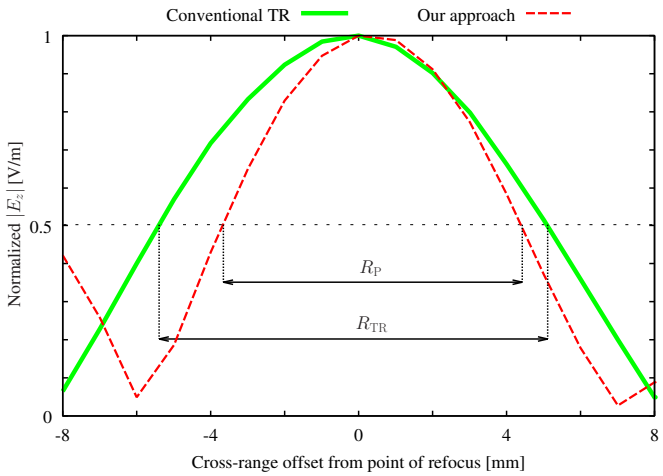

Fig. 6. Cross sections of the normalized $|E_z|$ distribution along the cross-range axis of refocusing after applying our approach, and without applying any resolution enhancement method.

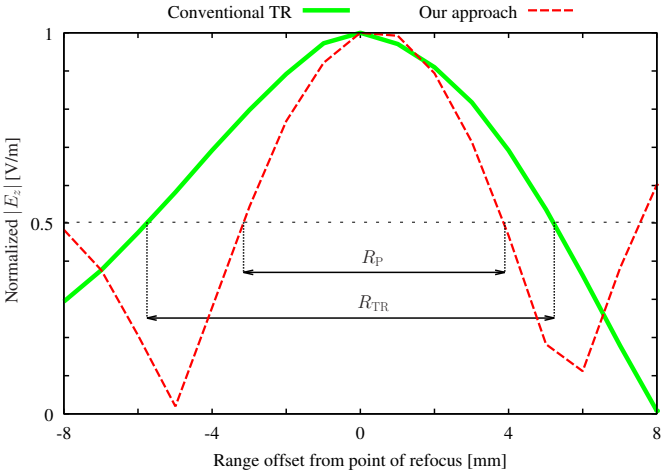

Fig. 7. Cross sections of the normalized $|E_z|$ distribution along the range axis of refocusing after applying our approach, and without applying any resolution enhancement method.

tion along the cross-range and range directions respectively. Symbols R_{TR} and R_{P} represent the resolution of the spatial focusing at the time of refocusing, using no resolution enhancement method (R_{TR}), and using the proposed resolution enhancement approach (R_{P}) respectively. We measure the range and cross-range resolutions of R_{TR} and R_{P} as the minimum distance between two half-maxima in $|E_z|$ nearest the point of refocusing, along the range and cross-range directions respectively, as in [22].

The method in [22] generates the peak of the backpropagated $|E_z|$ signal near the TRA and hence breaks the TR refocusing process. Along the range direction, our method outperforms the conventional TR method in precision by a factor of $R_{\mathrm{TR}}/R_{\mathrm{P}} = 1.56$. Along the cross-range direction, our method provides $R_{\mathrm{TR}}/R_{\mathrm{P}} = 1.3$ times better resolution than the unfiltered TR approach. Along the range direction, it is $R_{\mathrm{P}} = 7.03\,\mathrm{mm}$ and $R_{\mathrm{TR}} = 10.98\,\mathrm{mm}$. Hence, the range precision of the proposed method is approximately equal to the ground-truth tumor's size, whereas the precision of the conventional TR approach is 1.57 times coarser than the tumor's size. We did not compare the refocusing resolution achieved using our approach with the results using [22], since there is no refocusing with the approach in [22].

IV. Conclusion

The time reversal invariance of the wave equation is broken in dispersive media such as human tissues. The method in [22] provides an adaptive-window approach for inverse filters in the wavelet domain, without requiring the realization of prior experiments. However, the algorithm in [22] only considers propagation at the center frequency of the interrogating pulse through the dispersive media. In addition, the wavelet-domain model for the attenuation used by [22] does not relate the wavelet transform's scales to frequencies correctly, and is thus unreliable. Our work corrected and improved the method in [22]. Our algorithm for the resolution enhancement of TR microwave imaging employed the frequency-dependent complex permittivity of the propagation medium across the *whole* spectrum of interest, for the computation of the attenuation which the interrogating UWB pulse undergoes during TR forward propagation. Our algorithm also introduced a smart selection of scales on which to obviate the inverse filtering process, to minimize undesired noise amplification, contrary to the empirical approaches in relevant prior work. Further, we integrated the minimum entropy selection to dispersion compensation problems for the first time to our knowledge, to determine the time of TR refocusing. We applied our method to a three-dimensional scenario involving a brain tumor inside the head of a DHP. Our approach improved the refocusing resolution of the conventional TR approach, while prior work failed to refocus at the tumor. One limitation that the simulations in this work share with prior work is that they do not take into account effects due to finite dipole size or mutual coupling between the TRA elements. This is because the main aim of this work is the development of the resolution enhancement algorithm. Furthermore, we currently do not have an experimental setup. However, we considered a computational setup which is similar to setups found in head imaging literature [51]–[53]. As a part of future work based upon this study, more realistic simulation models or practical experiments can be developed to assess any possible impact these effects have on the microwave imaging. Note also that, while we have considered the resolution enhancement of brain imaging as our case study, the introduced algorithm is general and can be applied in other applications, such as GPR applications, through-the-wall imaging, as well as purely computational methods. Also, similarly to the prior work, this paper assumes that the time-reversal of the exact perturbed field due to the target is possible by perfect background subtraction, which may not be a trivial process in some real-world applications where the background's response may not be readily available. However, the simulation experiments presented in this work suffice to demonstrate the performance of our new TR imaging resolution enhancement approach relative to the prior work and the conventional TR method

for UWB propagation in heterogeneous and dispersive environments. Future research also includes the integration of the proposed algorithm with clutter removal techniques, the assessment of the statistical characteristics of our method in random media, and of its imaging performance when applied on other TR-based techniques, such as the UWB-MUltiple SIgnals Classification (MUSIC) method, as well as extensions to other disciplines involving dispersive media.

APPENDIX
RELATING WAVELET SCALES TO FOURIER FREQUENCIES

Wavelet scales are not *per se* related to frequencies analyzed by the wavelet transform, but rather define a stretch of the wavelet function in time domain. For cases where the mother wavelet contains dominant periodic components, an analytical relation can be found between each wavelet scale and one equivalent Fourier frequency. We derive (14), which relates each wavelet transform scale factor to one equivalent Fourier frequency using the complex Morlet mother wavelet, following the approach in [30] (which relates wavelet scale factors to equivalent Fourier wavelengths). The principle of this approach is that a monochromatic wave at a known frequency maximizes the wavelet energy density at the scale associated to this frequency.

Let $f(t)$ be a complex sinusoid of known frequency ω_r and $\hat{f}(\omega)$ denote the Fourier transform of $f(t)$, then

$$\begin{aligned} f(t) &= e^{\jmath\omega_\mathrm{r} t} \\ \therefore \hat{f}(\omega) &= 2\pi\delta(\omega-\omega_\mathrm{r}) \end{aligned} \tag{24}$$

where $\delta(\ )$ is the Dirac delta function. The complex Morlet wavelet is expressed in frequency domain as

$$\hat{\psi_0}(\omega) = \pi^{1/4}\sqrt{2}e^{-\frac{1}{2}(\omega-\omega_\mathrm{M})^2}. \tag{25}$$

We take the CWT of $f(t)$ using its frequency domain representation, employing $\psi_0(t)$ as the mother wavelet at scale factor a and with a translation in time of b temporal units:

$$T(a,b) = \sqrt{a}\int_{-\infty}^{\infty} \hat{f}(\omega)\hat{\psi_0}^*(a\omega)e^{\jmath\omega b}\,\mathrm{d}\omega. \tag{26}$$

Substituting $\hat{f}(\omega)$ in (24) and $\hat{\psi_0}(a\omega)$ in (25) into (26), we obtain

$$\begin{aligned} T(a,b) &= \sqrt{a}\int_{-\infty}^{\infty} 2\pi\delta(\omega-\omega_\mathrm{r})\pi^{1/4}\sqrt{2}e^{-\frac{1}{2}(a\omega-\omega_\mathrm{M})^2}e^{\jmath\omega b}\,\mathrm{d}\omega \\ &= 2\pi\sqrt{a}e^{\jmath\omega_\mathrm{r} b}\left(\pi^{1/4}\sqrt{2}e^{-\frac{1}{2}(a\omega_\mathrm{r}-\omega_\mathrm{M})^2}\right) \\ &= 2\pi\sqrt{a}e^{\jmath\omega_\mathrm{r} b}\hat{\psi_0}(a\omega_\mathrm{r}). \end{aligned}$$

The wavelet energy density function (also called the *wavelet power spectrum* by some authors [30], [54]) is

$$\begin{aligned} |T(a,b)|^2 &= 4\pi^2 a\left|\hat{\psi_0}(a\omega_\mathrm{r})\right|^2 \\ &= 4\pi^2\pi^{1/2}2ae^{-(a\omega_\mathrm{r}-\omega_\mathrm{M})^2} \end{aligned}$$

To derive the scale $a = a_\mathrm{r}$ where the wavelet energy density is maximized, we require

$$\left.\frac{\partial|T(a,b)|^2}{\partial a}\right|_{a=a_\mathrm{r}} = 0.$$

Therefore,

$$\begin{aligned} 4\pi^2\pi^{1/2}2e^{-(a_\mathrm{r}\omega_\mathrm{r}-\omega_\mathrm{M})^2}\left(-2{\omega_\mathrm{r}}^2a_\mathrm{r}^2+2a_\mathrm{r}\omega_\mathrm{r}\omega_\mathrm{M}+1\right) &= 0 \\ \therefore -2{\omega_\mathrm{r}}^2a_\mathrm{r}^2+2\omega_\mathrm{r}\omega_\mathrm{M}a_\mathrm{r}+1 &= 0. \end{aligned} \tag{27}$$

The accepted realistic root of the quadratic equation (27) is

$$a_\mathrm{r} = \frac{1}{2}\left[\frac{\omega_\mathrm{M}+\sqrt{2+{\omega_\mathrm{M}}^2}}{\omega_\mathrm{r}}\right] \tag{28}$$

since the rejected solution would suggest $a_\mathrm{r} < 0$. By setting $f_\mathrm{e}(\omega_\mathrm{M}, a)\triangleq\omega_\mathrm{r}/2\pi$ and $a\triangleq a_\mathrm{r}$ into (28) and rearranging, we obtain (14).

REFERENCES

[1] J. Jones, *Acoustical Imaging*, ser. Acoustical Imaging. Springer US, 2012, no. v. 21.

[2] V. R. N. Santos and F. L. Teixeira, "Application of time-reversal-based processing techniques to enhance detection of GPR targets," *J. Appl. Geophys.*, vol. 146, pp. 80 – 94, 2017.

[3] M. E. Yavuz and F. L. Teixeira, "Full time-domain DORT for ultra-wideband electromagnetic fields in dispersive, random inhomogeneous media," *IEEE Trans. Antennas Propag.*, vol. 54, no. 8, pp. 2305–2315, Aug. 2006.

[4] A. E. Fouda, F. L. Teixeira, and M. E. Yavuz, "Time-reversal techniques for MISO and MIMO wireless communication systems," *Radio Sci.*, vol. 47, no. 6, 2012.

[5] G. Lerosey, J. de Rosny, A. Tourin, A. Derode, G. Montaldo, and M. Fink, "Time reversal of electromagnetic waves and telecommunication," *Radio Sci.*, vol. 40, no. 6, 2005.

[6] D. Liu, G. Kang, L. Li, Y. Chen, S. Vasudevan, W. Joines, Q. H. Liu, J. Krolik, and L. Carin, "Electromagnetic time-reversal imaging of a target in a cluttered environment," *IEEE Trans. Antennas Propag.*, vol. 53, no. 9, pp. 3058–3066, 2005.

[7] L. El Sahmarany, L. Berry, N. Ravot, F. Auzanneau, and P. Bonnet, "Time reversal for soft faults diagnosis in wire networks," *Prog. Electromagn. Res. M*, vol. 31, pp. 45–58, 2013.

[8] V. C. Odedo, M. E. Yavuz, F. Costen, R. Himeno, and H. Yokota, "Time reversal technique based on spatiotemporal windows for through the wall imaging," *IEEE Trans. Antennas Propag.*, vol. 65, no. 6, pp. 3065–3072, Jun. 2017.

[9] C. Zhang, Y. Kuga, and A. Ishimaru, "Hard-wall radar imaging: Localization of objects shadowed by metallic walls with MIMO radar," *IEEE Trans. Antennas Propag.*, vol. 66, no. 8, pp. 4240–4251, Aug. 2018.

[10] R. C. Qiu, C. Zhou, N. Guo, and J. Q. Zhang, "Time reversal with MISO for ultrawideband communications: Experimental results," *IEEE Antennas Wireless Propag. Lett.*, vol. 5, pp. 269–273, 2006.

[11] Y. Chen, Y. Yang, F. Han, and K. J. R. Liu, "Time-reversal wideband communications," *IEEE Signal Process. Lett.*, vol. 20, no. 12, pp. 1219–1222, Dec. 2013.

[12] H. T. Nguyen, I. Z. Kovcs, and P. C. F. Eggers, "A time reversal transmission approach for multiuser UWB communications," *IEEE Trans. Antennas Propag.*, vol. 54, no. 11, pp. 3216–3224, Nov. 2006.

[13] S. Mukherjee, L. Udpa, S. Udpa, E. J. Rothwell, and Y. Deng, "A time reversal-based microwave imaging system for detection of breast tumors," *IEEE Trans. Microw. Theory Techn.*, vol. 67, no. 5, pp. 2062–2075, May 2019.

[14] P. Takook, H. Dobsicek Trefna, X. Zeng, A. Fhager, and M. Persson, "A computational study using time reversal focusing for hyperthermia treatment planning," *Prog. Electromagn. Res. B*, vol. 73, pp. 117–130, 2017.

[15] M. D. Hossain and A. S. Mohan, "Cancer detection in highly dense breasts using coherently focused time-reversal microwave imaging," *IEEE Trans. Comput. Imag.*, vol. 3, no. 4, pp. 928–939, 2017.

[16] P. Kosmas and C. M. Rappaport, "Time reversal with the FDTD method for microwave breast cancer detection," *IEEE Trans. Microw. Theory Techn.*, vol. 53, no. 7, pp. 2317–2323, Jul. 2005.

[17] P. Kosmas and C. M. Rappaport, "A matched-filter FDTD-based time reversal approach for microwave breast cancer detection," *IEEE Trans. Antennas Propag.*, vol. 54, no. 4, pp. 1257–1264, 2006.

[18] M. D. Hossain, A. S. Mohan, and M. J. Abedin, "Beamspace time-reversal microwave imaging for breast cancer detection," *IEEE Antennas Wireless Propag. Lett.*, vol. 12, pp. 241–244, 2013.

[19] M. E. Yavuz and F. L. Teixeira, "Frequency dispersion compensation in time reversal techniques for UWB electromagnetic waves," *IEEE Geosci. Remote Sens. Lett.*, vol. 2, no. 2, pp. 233–237, Apr. 2005.

[20] M. Pastorino and A. Randazzo, *Microwave Imaging Methods and Applications*, ser. Artech House microwave library. Artech House, 2018.

[21] A. M. Abduljabbar, M. E. Yavuz, F. Costen, R. Himeno, and H. Yokota, "Frequency dispersion compensation through variable window utilization in time-reversal techniques for electromagnetic waves," *IEEE Trans. Antennas Propag.*, vol. 64, no. 8, pp. 3636–3639, Aug. 2016.

[22] ——, "Continuous wavelet transform-based frequency dispersion compensation method for electromagnetic time-reversal imaging," *IEEE Trans. Antennas Propag.*, vol. 65, no. 3, pp. 1321–1329, Mar. 2017.

[23] L. Peretto, R. Sasdelli, and R. Tinarelli, "Uncertainty propagation in the discrete-time wavelet transform," *IEEE Trans. Instrum. Meas.*, vol. 54, no. 6, pp. 2474–2480, 2005.

[24] M. J. Shensa, "The discrete wavelet transform: wedding the À Trous and Mallat algorithms," *IEEE Trans. Signal Process.*, vol. 40, no. 10, pp. 2464–2482, 1992.

[25] C. Torrence and G. P. Compo, "A practical guide to wavelet analysis," *B. Am. Meteorol. Soc.*, vol. 79, no. 1, pp. 61–78, 1998.

[26] M. Farge, "Wavelet transforms and their applications to turbulence," *Annual review of fluid mechanics*, vol. 24, no. 1, pp. 395–458, 1992.

[27] P. S. Addison, *The Illustrated Wavelet Transform Handbook: Introductory Theory and Applications in Science, Engineering, Medicine and Finance, Second Edition*. CRC Press, 2017.

[28] R. Hu, V. Monebhurrun, R. Himeno, H. Yokota, and F. Costen, "An adaptive least angle regression method for uncertainty quantification in FDTD computation," *IEEE Trans. Antennas Propag.*, vol. 66, no. 12, pp. 7188–7197, Dec. 2018.

[29] C. Johnk, *Engineering Electromagnetic Fields and Waves*. Wiley, 1988.

[30] S. D. Meyers, B. G. Kelly, and J. J. O'Brien, "An introduction to wavelet analysis in oceanography and meteorology: With application to the dispersion of Yanai waves," *Mon. Weather Rev.*, vol. 121, no. 10, pp. 2858–2866, 1993.

[31] E. Sitnikova, A. E. Hramov, A. A. Koronovsky, and G. van Luijtelaar, "Sleep spindles and spike–wave discharges in EEG: Their generic features, similarities and distinctions disclosed with Fourier transform and continuous wavelet analysis," *J. Neurosci. Meth.*, vol. 180, no. 2, pp. 304 – 316, 2009.

[32] Y. Wang, "Q analysis on reflection seismic data," *Geophys. Res. Lett.*, vol. 31, no. 17, 2004.

[33] I. L. S. Braga and F. S. Moraes, "High-resolution gathers by inverse Q filtering in the wavelet domain," *GEOPHYSICS*, vol. 78, no. 2, pp. V53–V61, 2013.

[34] Y. Wang, "Inverse Q -filter for seismic resolution enhancement," *GEOPHYSICS*, vol. 71, no. 3, pp. V51–V60, 2006.

[35] ——, *Seismic Inverse Q Filtering*. Wiley, 2009.

[36] K. Aldape, K. M. Brindle, L. Chesler, R. Chopra, A. Gajjar, M. R. Gilbert, N. Gottardo, D. H. Gutmann, D. Hargrave, E. C. Holland *et al.*, "Challenges to curing primary brain tumours," *Nat. Rev. Clin. Oncol.*, vol. 16, no. 8, pp. 509–520, 2019.

[37] R. L. Siegel, K. D. Miller, and A. Jemal, "Cancer statistics, 2016," *CA-Cancer J. Clin.*, vol. 66, no. 1, pp. 7–30, 2016.

[38] E. J. Joseph, K. A. H. Ping, K. Kipli, D. A. A. Mat, S. Sahrani, D. N. A. Zaidel, M. I. Sariphn, and M. H. Marhaban, "Integration of image segmentation method in inverse scattering for brain tumour detection," *Prog. Electromagn. Res.*, vol. 61, pp. 111–122, 2017.

[39] T. Wuren, T. Takai, M. Fujii, and I. Sakagami, "Effective 2-debye-pole FDTD model of electromagnetic interaction between whole human body and UWB radiation," *IEEE Microw. Wireless Compon. Lett.*, vol. 17, no. 7, pp. 483–485, Jul. 2007.

[40] C. Gabriel, S. Gabriel, and y. E. Corthout, "The dielectric properties of biological tissues: I. Literature survey," *Phys. Med. Biol.*, vol. 41, no. 11, p. 2231, 1996.

[41] S. Gabriel, R. Lau, and C. Gabriel, "The dielectric properties of biological tissues: II. Measurements in the frequency range 10 Hz to 20 GHz," *Phys. Med. Biol.*, vol. 41, no. 11, p. 2251, 1996.

[42] RIKEN, Wako Saitama, Japan, "Media parameters for the Debye relaxation model," http://cfd-duo.riken.jp/cbms-mp/, [Online; accessed 20-February-2020].

[43] P. Cignoni, M. Callieri, M. Corsini, M. Dellepiane, F. Ganovelli, and G. Ranzuglia, "Meshlab: an open-source mesh processing tool," in *Eurographics Italian Chapter Conf.*, V. Scarano, R. D. Chiara, and U. Erra, Eds. The Eurographics Association, 2008.

[44] M. Kazhdan and H. Hoppe, "Screened Poisson surface reconstruction," *ACM Trans. Graphics (TOG)*, vol. 32, no. 3, p. 29, 2013.

[45] O. P. Gandhi, B. Gao, and J. Chen, "A frequency-dependent finite-difference time-domain formulation for general dispersive media," *IEEE Trans. Microw. Theory Techn.*, vol. 41, no. 4, pp. 658–665, Apr. 1993.

[46] J. P. Bérenger, "Numerical reflection from FDTD-PMLs: a comparison of the split PML with the unsplit and CFS PMLs," *IEEE Trans. Antennas Propag.*, vol. 50, no. 3, pp. 258–265, Mar. 2002.

[47] D. Yoo, "The dielectric properties of cancerous tissues in a nude mouse xenograft model," *Bioelectromagnetics*, vol. 25, no. 7, pp. 492–497, 2004.

[48] P. Kosmas and C. M. Rappaport, "FDTD-based time reversal for microwave breast cancer detection-localization in three dimensions," *IEEE Trans. Microw. Theory Techn.*, vol. 54, no. 4, pp. 1921–1927, 2006.

[49] Y. Jin and J. M. F. Moura, "Imaging by time reversal beamforming," Dec. 11 2012, US Patent 8,330,642.

[50] S. Mukherjee, L. Udpa, S. Udpa, and E. J. Rothwell, "Target localization using microwave time-reversal mirror in reflection mode," *IEEE Trans. Antennas Propag.*, vol. 65, no. 2, pp. 820–828, 2016.

[51] M. Ojaroudi, S. Bila, and M. Salimi, "A Novel Approach of Brain Tumor Detection using Miniaturized High-Fidelity UWB Slot Antenna Array," *13th European Conf. on Antennas Propag., EuCAP 2019*, no. EuCAP, 2019.

[52] M. S. R. Bashri, T. Arslan, W. Zhou, and N. Haridas, "Wearable device for microwave head imaging," in *2016 46th European Microwave Conf. (EuMC)*. IEEE, Oct. 2016, pp. 671–674.

[53] M. S. R. Bashri, T. Arslan, and W. Zhou, "Flexible antenna array for wearable head imaging system," in *2017 11th European Conf. on Antennas Propag. (EUCAP)*. IEEE, Mar. 2017, pp. 172–176.

[54] M.-C. Huang, "Wave parameters and functions in wavelet analysis," *Ocean Eng.*, vol. 31, no. 1, pp. 111 – 125, 2004.